ADVANCED MATERIALS INTERFACES
Open Access
www.advmatinterfaces.de

P3HT-Based Electroactive Films for In Vitro Neuronal Cell Interfacing

Paola Campione, Claudia Latte Bovio, Giovanna Calabrese, Francesca Santoro, and Grazia Maria Lucia Messina**

Numerous efforts have been made to address the mechanical mismatch between bioelectronic devices and tissues in the past few years. Interfaces that better mimic the properties of biological tissues can be produced with the support of organic materials, which have a unique combination of soft mechanical properties, biocompatibility, and ionic-electronic conduction, which match the properties of living systems and allow the signal to be transduced at the biotic–abiotic interface. In this context, Poly(3-hexylthiophene) (P3HT), a p-type semiconducting polymer, having good biocompatibility, electrical conductivity, and mechanical properties, is studied. In this work, a polymer blend of P3HT and multi-walled carbon nanotubes (MWCNT) is prepared and deposited on the surface as an electroactive thin film resulting in a tunable nanostructured surface. Further, the biological properties of this new substrate in vitro is evaluated. The conductive polymer-based substrate and the HT-22 cell line can be better connected because of this nanostructured surface effect on the cells' responses to local changes in curvature and topography of the materials. This model is simple yet effectively shows the investigation of neuronal responses to morphological characteristics and electronic interfaces.

1. Introduction

In the promising field of bioelectronics, the combination of electronics and biology has paved the way for new applications in many medical fields, including implantable devices.[1] Central to this interdisciplinary effort to overcome the gap between technology and biology, is the seamless tissue-device integration.[2] In the last years, significant efforts have been undertaken to address the drawbacks associated with the mechanical mismatch between bioelectronics device and tissue. This has been achieved through the use of flexible and biocompatible polymer substrates, which aim to prevent inflammatory responses and potential damage to the tissue.[3] Based on this evidence, researchers have increasingly turned their attention to organic bioelectronics as a promising avenue to address these limitations.[4–9] Organic materials have proven advantageous in producing interfaces that better mimic the properties of biological tissues.[10,11] Moreover, they offer a unique combination of soft mechanical properties, biocompatibility, and ionic-electronic conduction,[6,12,13] matching the properties of living systems and allowing a better transduction of the signal at the biotic-abiotic interface. In the realm of organic bioelectronics, neuroelectronics have attracted growing interest. The integration of organic materials with neuroelectronics has paved the way for exciting new possibilities of exploration, particularly in the study

P. Campione, G. M. L. Messina
Laboratory for Molecular Surface and Nanotechnology (LAMSUN)
Department of Chemical Sciences
University of Catania and CSGI
Viale A. Doria, 6, Catania 95125, Italy
E-mail: gml.messina@unict.it

C. Latte Bovio, F. Santoro
Tissue Electronics
Istituto Italiano di Tecnologia
Naples 80125, Italy
E-mail: f.santoro@fz-juelich.de

The ORCID identification number(s) for the author(s) of this article can be found under https://doi.org/10.1002/admi.202400776

DOI: 10.1002/admi.202400776

C. Latte Bovio
Dipartimento di Chimica, Materiali e Produzione Industriale
Università di Napoli Federico II
Naples 80125, Italy

G. Calabrese
Department of Chemical
Biological
Pharmaceutical and Environmental Sciences (ChiBioFarAm)
University of Messina
Messina 98166, Italy

F. Santoro
Faculty of Electrical Engineering and IT
RWTH Aachen
52074 Aachen, Germany

F. Santoro
Institute for Biological Information Processing-Bioelectronics
Forschungszentrum Jülich
52428 Jülich, Germany

of neuronal cell cultures and their innovative applications.[14–16] This synergy holds promise for decoding the complexities of neural networks and advancing the development of neuroprosthetic devices. In the recent years, conductive polymers (CPs) have attracted great consideration in neuroelectronic field. This interest is largely due to their straightforward manufacturing process, good conductivity, cost-effectiveness, biocompatibility, and environmental stability.[17,18] Among these the Poly(3-hexylthiophene) (P3HT) has emerged prominently. P3HT, a p-type semiconducting polymer, has been used in tissue engineering applications as a neural scaffold material due to its biocompatibility, good electrical conductivity, and mechanical properties.[19]

A complete characterization of the polymer–liquid interface is essential for enhancing all related devices. Mainstream studies focused on examining the impact of water contaminants on the deterioration of the organic layer. According to existing literature, a charge transfer complex is formed between P3HT and molecular oxygen, characterized by a positive partial charge mainly localized on the polymer backbone. This behavior mirrors the emergence of polaronic species within P3HT. Additionally, the presence of water affects P3HT by polarizing the polymer surface, resulting in a shift of the electronic energy levels in the outermost layer to lower energies. Consequently, the incorporation of molecular oxygen onto this hydrated polymer surface becomes energetically favorable. Furthermore, the saline solution utilized in cell culture promotes the formation of localized electrical dipoles within the charge transfer complex. The presence of oxygen within the van der Waals radius of the polymer chain further enhances weak charge transfer reactions.[20,21]

In this study, we investigated the biological properties of a P3HT-based substrate in vitro, in terms of cell adhesion, proliferation and biocompatibility, for medical device applications.

The use of polymeric blends of P3HT and multi-walled carbon nanotubes (MWCNT) has led to the formation of a P3HT-based substrate with a tunable nanostructured surface. Research has shown that nanostructuring of surfaces significantly influences cell behavior, moving from conventional 2D cell cultures to pseudo-3D interfaces. This progress is crucial for developing more effective bio interfaces for in vitro applications.[22–28] By varying the nanostructure of surfaces is possible to stimulate cellular responses to localized changes in curvature and topography of the materials, thereby enhancing the interactions between the CP-based substrate and the biological components.[29–34]

In this study, the HT-22 cell line[35] was used, because of its similarities with primary neurons, providing a simplified yet representative model to investigate neuronal response to morphological features and electronic interfaces. HT-22 cells offer several significant advantages, including their capacity for neurite outgrowth through differentiation. This characteristic facilitates the investigation of how the topographical properties of the materials used as substates influence cell behavior. Additionally, their ability to establish functional synapses paves the way for simulating and examining synaptic connectivity in response to electronic stimuli. These characteristics make them the perfect candidate for this study aimed at exploring the effects of nanostructured surfaces on neuronal cell adhesion and proliferation, alongside the conductive properties of the polymeric matrix that promote effective network development. In particular, to promote cell adhesion and improve cell-chip interaction, the adsorption process of Poly-L-lysine (PLL),[36] which serves as a protein coating – has been explored at the interface of P3HT and P3HT-MWCNT thin films. Enhancing the interaction between of HT-22 cells and P3HT-MWCNT surfaces essentially optimizing cell-chip coupling – and probing how the pseudo 3D nanostructured surface influences cellular behavior is a crucial advancement. This understanding plays a key role in the creation of biocompatible and functional interfaces, which have significant potential for future applications in neuroelectronics, bioelectronics, and tissue engineering.

2. Results and Discussion

2.1. Surface Characterization

The topography of the P3HT pristine (**Figure 1a**) and blend P3HT-MWCNT (Figure 1b) films has been analysed by mean of atomic force microscopy (AFM) in tapping mode. The P3HT film shows a smooth, flat surface, while the polymer blend exhibits a consistent dispersion of the MWCNTs filler throughout the polymeric matrix. Additionally, it's noteworthy that the blend displays a three dimensional "spaghetti like" morphology (Figure S1a,b, Supporting Information).[37] The roughness data presented in Figure 1c, show that the incorporation of carbon nanotubes significantly improves the average roughness of the samples, increasing it by over an order of magnitude. Moreover, the formation of the blend with MWCNTs has an impact on the mechanical properties of the layer at the nanometer scale. Accordingly, the elastic response of the materials was measured by means of nanoindentation with AFM. From the collected force-distance curves, Young Modulus values were obtained by fitting the slope in the elastic region with the Derjaguin, Muller, Toporov (DMT) model and they are reported in Figure 1c. P3HT-MWCNT thin films exhibit a lower Young's modulus, a characteristic linked to the structural arrangement of MWCNTs at the surface, which create a "cushion effect". This unique structure not only softens the film but also minimizes the mechanical mismatch between the material and the biological systems, enabling improved interaction with cells.[38–41] Figure 1d shows the voltammograms of P3HT and P3HT-MWCNT films in PBS. It is noteworthy that there is a significant difference in the intensity of the current peaks; the blend films exhibit both higher intensity and greater conductivity compared to the pristine P3HT polymer films. Analyzing the curve area reveals that the capacitance of the systems is $4.17 \times 10^{-5} \pm 0.76 \times 10^{-5}$ F for the P3HT film and $4.92 \times 10^{-4} \pm 0.76 \times 10^{-4}$ F for the P3HT-MWCNT composites. This indicates a significant difference of approximately one order of magnitude between the two samples, which can be attributed to the inclusion of the MWCNTs as a filler. The voltammograms of P3HT (Figure 1d inset) show two distinct peaks: an oxidation peak at approximately 1.4 V and reduction peak at around 1 .2V. The calculated energy gap is 1.94 ± 0.01 eV, which is consistent with value reported in the literature.[42–44] In contrast, P3HT-MWCNT sample displays only a reduction peak, with no accompanying oxidation peak. This phenomenon could be attributed to the occupation of the lower unoccupied molecular orbital (LUMO) by electrons provided by MWCNTs. The current-voltage (IV) curves (Figure S1c,d, Supporting Information) obtained from

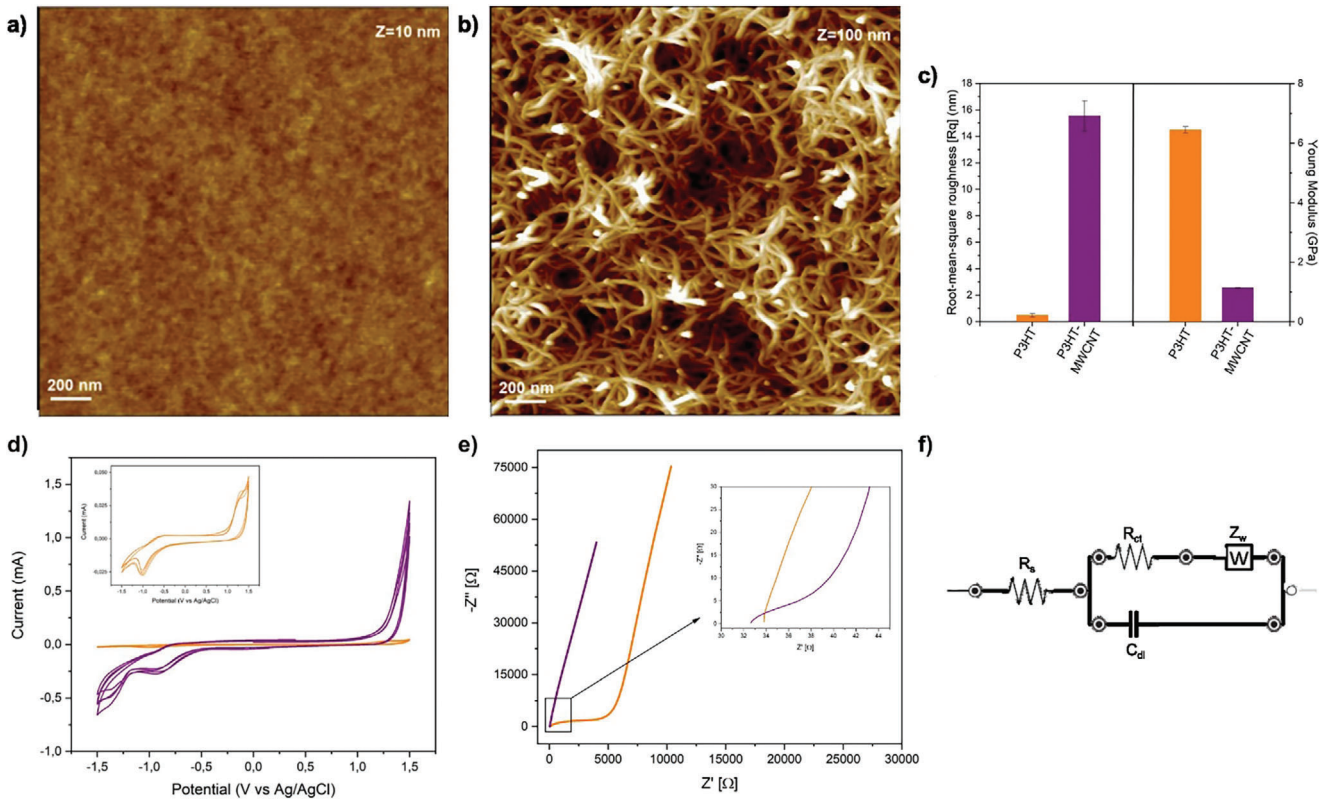

Figure 1. Surfaces characterization. a) tapping mode atomic force micrographs of P3HT film and b) P3HT-MWCNT blend; c) Root mean squared roughness (Rq), and Young Modulus values; d) Cyclic voltammograms of P3HT (in orange) and P3HT-MWCNT (in purple) in PBS. Inset: zoom of voltammogram of P3HT. e) Electrochemical impedance spectroscopy (EIS) of P3HT on ITO (in orange) and P3HT-MWCNT on ITO (in purple) in PBS. Inset: zoom at higher frequencies. f) Randles equivalent circuit used for the model of the systems.

conductive atomic force microscopy (c-AFM) measurements in the air, clearly indicate that the carbon nanotubes effectively filled the energy gap, revealing both the absence of this gap and a current region at 0A. Moreover, an analysis of the first derivative of the IV curves exhibited a pronounced peak between 2 and 4 V for P3HT, while the P3HT-MWCNT blend displayed a peak in the range of −0.02V–0 .02V. The calculated conductance values were found to be 7.90 ± 0.03 nS for P3HT and significantly higher 6231.93 ± 789.58 nS for P3HT-MWCNT. These results strongly confirm the enhanced conductivity of the polymer blend, which can be attributed to the presence of MWCNTs that facilitate the formation of an effective conductive network within the semiconducting polymer matrix.

Furthermore, designing a platform for cell sensing and stimulation requires a low electrode-electrolyte impedance interface. This is essential for ensuring good sensitivity and achieving a high signal-to noise ratio for the recorded neural signals, which typically measure in microvolts range. This is particularly important given the electrical fluctuations associated with the electrode's environment.[45] To investigate this, we conducted electrochemical impedance spectroscopy (EIS) on the systems using phosphate-buffered saline solution (PBS) as the electrolyte. This analysis covered a frequency range from 1 MHz to 0.1 Hz with a potential amplitude of 50 mV. The resulting Nyquist plots are presented in Figure 1e. To fully understand the physical processes that influence impedance, equivalent circuit models have long been used to model these systems using electrical elements. The widely recognized Randles circuit,[46] reported in Figure 1f, includes an electrolyte resistance (R_s) in series with a parallel arrangement of an interface capacitance (C_{dl}) resulting from due to the double layer formation, alongside a charge transfer resistance (R_{ct}) combined with a diffusional resistance element represented by the Warburg impedance (Z_W). This model has been employed to analyse and fit the data acquired from the EIS measurements, as shown in Figure S1e,f (Supporting Information). The plot clearly shows a significant disparity in the charge transfer resistance (R_{ct}) between the two electrodes. Specifically, the P3HT-MWCNT substrate exhibits a remarkable reduction in resistance by two orders of magnitude. Additionally, there is also an observed increase in the capacitance, which further corroborates the findings from the previous cyclic voltammetry (CV) measurements. The impedance of blend P3HT-MWCNT composite thin films significatively decrease due to two key reasons: the increased electroactive area resulting from greater surface roughness and the enhanced conductivity of the film attributed to the MWCNT network embedded within the polymer matrix.

2.2. Protein Adsorption on Surfaces: Quantities and Kinetics

Figure 2 shows the amount of PLL adsorbed as well as the adsorption kinetics on P3HT (depicted in orange) and on

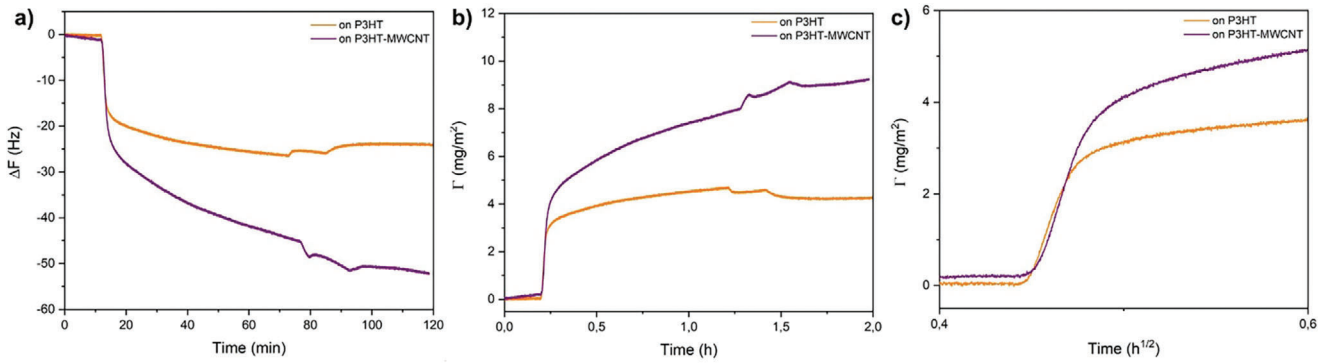

Figure 2. Protein adsorption and kinetics. a) Frequency shift plot of PLL adsorption on P3HT film (orange line) and P3HT-MWCNT film (purple line) by quartz crystal microbalance with dissipation monitoring (QCM-D); b) related adsorption kinetics onto the different substrates, c) zoom in on adsorption kinetics of first few minutes.

P3HT-MWCNT (shown in purple) surfaces, all studied by using the quartz crystal microbalance with dissipation monitoring (QCM-D) technique. The frequency shifts (Δf) were recorded after each step of adsorption until the steady state was achieved. Notably, a remarkable difference in protein adsorption was observed between the two different substrates (Figure 2a). This variation can be attributed to the roughness of the blend polymer film, which increases the surface area and, in turn, enhances the amount of mass that can be adsorbed. After the rinsing steps with buffer solution at 70 and 85 min, no significant desorption is observed on either substrate, indicating the formation of a stable protein layer on the surface. In both the measurements, there was no significant spread in the overtones, which collapsed into a very narrow range, along with the corresponding dissipation (see Figure S2a,b, Supporting Information). This behavior suggests the formation of a rigid and thin layer, allowing for the application of the Sauerbrey equation to assess the frequency-mass relationship. The calculated adsorbed mass and the number of molecules at surface are reported in **Table 1**.

Additional insights into the kinetics of the adsorption process could be obtained by analysing the plots of dissipation shift (ΔD) versus Δf reported in Figure S2c (Supporting Information). These plots reveal two distinct kinetics steps: the initial, rapid phase associated with the diffusion to the surface, followed by a slower phase that involves the reorganization of PLL at the interface. Figure 2b shows the curves depicting mass uptake on the substrate, while Figure 2c offers a closer look at the initial stages of adsorption during the early measurement period. This zoomed-in view highlights the transport of the protein from the bulk solution to the surfaces. Comparing the adsorption curves for the two different substrates, it is evident that the transport process occurs more rapidly in the P3HT-MWCNT film compared to the pristine P3HT film. Utilizing random sequential analysis (RSA) enables the calculation of the apparent diffusion coefficient (S) along with the related average mass transfer rate constant (k_c) for the adsorption process. The coefficient S is determined from the slope of the diffusion-controlled step, based on the following Equation (1):[47]

$$\Gamma(t) = \frac{2}{\sqrt{\pi}} C_{bulk} \sqrt{S} \sqrt{t} \quad (1)$$

in which Γ is the mass uptake, C denotes the bulk concentration and t indicates the time.

The constant k_c represents the efficiency of protein mass transport driven by convection and its binding to the surfaces. This value can be calculated using the following Equation (2):[48]

$$k_c = C_f \, Q^{\frac{1}{3}} \, S^{\frac{2}{3}} \quad (2)$$

where Q is equal to 1.7×10^{-3} cm^3 s^{-1} and corresponds to the volumetric flow rate used for the measurements, $C_f = 19.9$ cm$^{-4/3}$ is a constant that depends on geometrical factors of the QCM-D cell and is independent from solution concentration, molecule size and flow rate, and S is the diffusion coefficient previously calculated.

Table 1 summarizes the values of the kinetic constants calculated for both analyzed substrates. The results reveal distinct kinetics behaviors; notably, the diffusion coefficient is higher in the blend polymer film compared to P3HT, indicating that the diffusion process at the interface occurs more rapidly in the blend. Conversely, the k_c values remain comparable across both substrates.

Table 1. Adsorption quantities and kinetics constants. Frequency and dissipation shifts, adsorbed mass, number of molecules per cm^2, apparent coefficient diffusion (S), and mass transfer rate constant (Kc) for PLL adsorption on P3HT and P3HT-MWCNT.

PLL adsorption	ΔF [Hz]	ΔD [10^{-6}]	Mass [ng cm^{-2}]	Molecule number/cm^2 [10^{12}]	S [cm^2 s^{-1}]	Kc [cm s^{-1}]
P3HT	−25.33 ± 1.66	0.98 ± 0.37	448.31 ± 29.34	1.20 ± 0.08	0.98×10^{-6}	0.23×10^{-3}
P3HT-MWCNT	−41.98 ± 1.09	0.91 ± 0.32	742.98 ± 19.27	1.99 ± 0.05	1.35×10^{-6}	0.29×10^{-3}

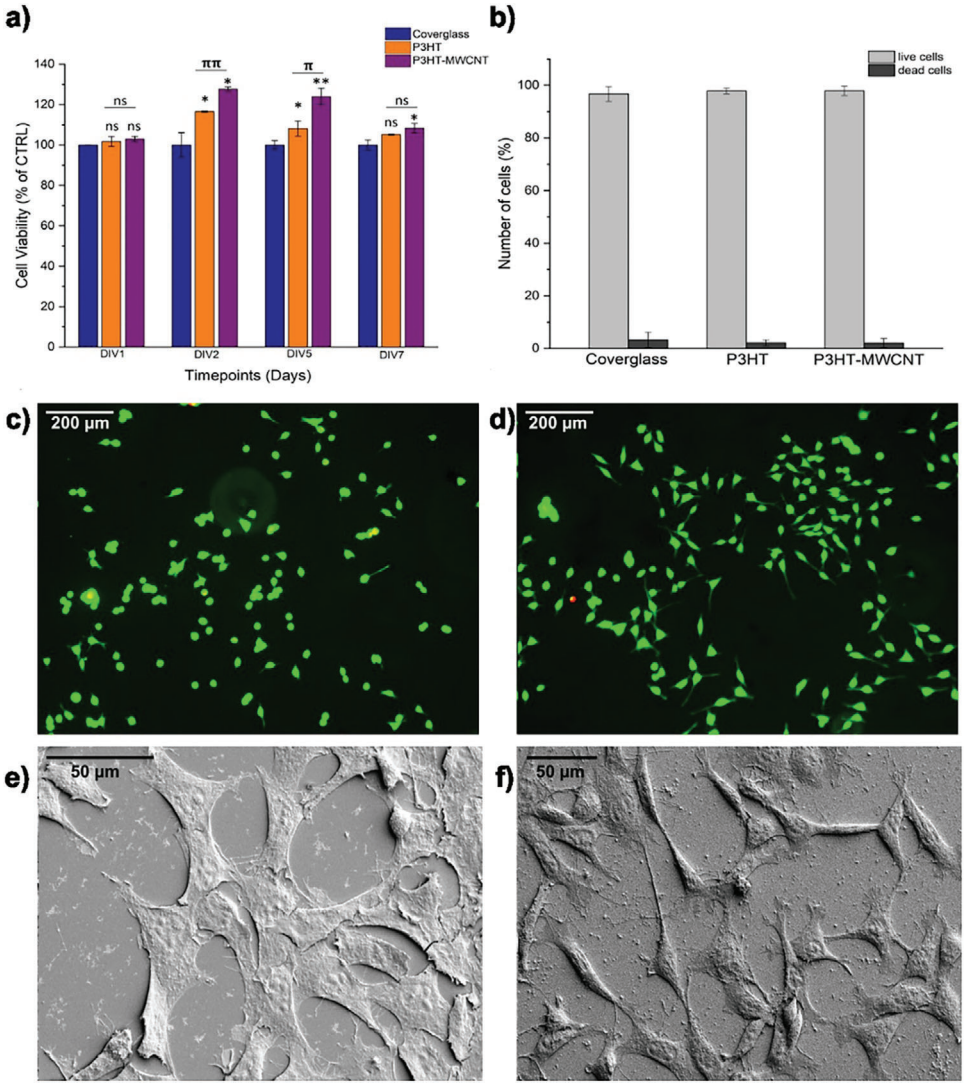

Figure 3. Biocompatibility and proliferation assay of HT-22 cells cultured on polymers films. a) Cell viability graph of HT-22 cells cultured on P3HT and P3HT-MWCNT compared to the control (coverglass), at different time points (DIV1, DIV2, DIV5, DIV7). Data are reported as mean ± standard deviation obtained from three different samples and three different experiments. * $p < 0.05$, ** $p < 0.01$ show significant differences between the two samples to the same timepoint, as reported by the ANOVA test: ns = not significant. b) Graph showing LIVE/DEAD analysis resulting from HT-22 cells cultured on P3HT and P3HT-MWCNT for 24h. c) LIVE/DEAD staining of HT-22 cells seeded on P3HT and d) on P3HT-MWCNT. Live cells are shown in green and dead cells in red. Scale bar, 200µm. Scanning electron microscopy (SEM) micrographs showing HT-22 cells cultured for 24 h on P3HT e) and P3HT-MWCNT f) respectively. Magnifications 2x (e) and 1.3x (f). Scale bar, 50 µm.

2.3. HT-22 Cultured on Surfaces

To evaluate the cytocompatibility of both P3HT and P3HT-MWCNT polymers with HT-22 cells, we performed a cell viability assay using MTT [3-(4,5-Dimethylthiazol-2-yl)-2,5-Diphenyltetrazolium Bromide] dye at different time points (1, 2, 5 and 7 days).[49] The absorbance value measured at 590 nm correlates strongly with the number of viable cells, enabling us to calculate the percentage of cell viability in comparison to the positive control (**Figure 3**a). Our data show that, at day in vitro 1 (DIV1), cell viability on P3HT and P3HT-MWCNT is comparable to that of the control (untreated coverglass). However, by DIV2 and DIV5, there is a significant increase in the number of live cells on both polymers, with P3HT-MWCNT exhibiting a greater enhancement than on P3HT. By DIV7, this trend persists among the different samples, although a decline in the number of live cells is observed due to the confluence of the cell layer on the samples. To further evaluate cell viability, we performed the live/dead fluorescence assay, after 1 day of HT-22 culture on the P3HT and P3HT-MWCNT polymers, and the results obtained align with those of the MTT test. Figure 3c,d provide a detailed view of cell viability on both polymers, showing that almost all cells grown on both polymers were viable. Most of the cells displayed green fluorescence, indicating that they were alive, while only a small number exhibited red fluorescence, signifying cell death. This observation is further supported by a calculated live cell percentage exceeding 96% (Figure 3b), which is comparable to the positive control demonstrated with glass samples

(Figure S3a, Supporting Information). These data show that both P3HT and P3HT-MWCNT polymers effectively promote the adhesion and proliferation of HT-22 cells. Additionally, scanning Electron Microscopy (SEM) micrographs show the spreading of HT-22 cells on the surfaces of P3HT and P3HT-MWCNT (Figure 3e,f).

The morphological characterization of HT-22 cells cultured on P3HT and P3HT-MWCNT substrates was performed using Immunofluorescence analysis (**Figure 4**a,b) and Scanning Electron Microscopy (SEM) (Figure 4c–f). Notably, a comparison of the fluorescence images, which display DAPI and Phalloidin staining, reveals that HT-22 cells grown on the P3HT-MWCNT substrate exhibit a distinct star-like and elongated neuronal morphology (Figure 4b). In contrast, the cells cultured on P3HT are smaller and adopt a rounded shape (Figure 4a). Fluorescent staining was performed to enhance the visibility of the cell membrane, as the quenching effect of MWCNT,[50,51] diminished the autofluorescence of P3HT. This reduction allowed for a clearer distinction of the HT-22 cells shape. SEM micrographs display the cell spreading and stretched morphology in both scenarios (Figure 4c,d). The high-magnification images (Figure 4e,f) further emphasize the adhesion of the filipodia on the HT-22 cells to both P3HT and the P3HT-MWCNT composite.

Nevertheless, there is no statistically relevant difference between the area and roundness values, calculated using ImageJ software, reported in violin plots in Figure 4g,h, also compared to the control (Figure S3b, Supporting Information).

Importantly, the contact area between HT-22 and the substrates was then visualized by means Scanning Electron Microscope-Focused Ion Beam (SEM-FIB) (**Figure 5**). In both P3HT (Figure 5a) and P3HT-MWCNT (Figure 5b), the cells exhibit strong adhesion to the substrates. Notably, the plasma membranes conform to the profiles of the materials, demonstrating effective interaction with the topographical features. The high magnification of the cross sections (Figure 5c,d) shows the significant impact of varying surfaces on the behavior of cell membranes. In the Figure 5c, it seems that the cell is firmly adhered to the P3HT surface, with the green stars indicating the presence of invagination. In contrast, the marked presence of the membrane invagination (noted by green stars) and membrane deformation (highlighted by the red line) in response to the "*spaghetti like*" surface (represented by the blue line) suggests that the HT-22 cells are actively interacting with the substrate.

Electrical cell-substrate impedance sensing (ECIS) is a label-free and non-invasive technique that has been used to provide information about live cells cultured on electrodes.[52,53] It allows to record information about cell growth or to monitor cell adhesion and proliferation. In this study, we employed electrochemical impedance spectroscopy (EIS), a technique that utilizes multiple-frequency spectroscopic measurements to assess different aspects of cell behavior.[54–57] In analyzing the cell-medium-electrode system, it is possible to distinguish three different contributions to impedance: interactions between cell, between cell and substrate and the impedance of the cell membrane itself. These contributions occur across varying frequency ranges, influenced by the underlying processes and the properties of the recording system. At high frequency, a significant capacitive coupling occurs between the current and the cell membranes, resulting in a decreased impedance of the cell layer. Therefore, monitoring cell behavior at high frequency proves essential for assessing processes related to the cell-electrode interactions, such as cell death, migration, proliferation, adhesion and spreading. Conversely, low-frequency currents are used to evaluate the stability and functional properties of adherent cells and tight junctions – two critical types of cell-cell interactions that play a vital role in regulating the flow of fluids, cells, and solutes across the cell layer. Additionally, in the intermediate frequency range, a complex network of potential pathways emerges, as the current operates through a combination of both cell-cell and cell-substrate interactions, each contributing differently to the overall impedance profile.

In order to verify the suitability and the efficiency of our substrates for bioelectronic applications, we performed EIS measurements on P3HT and P3HT-MWCNT deposited onto indium tin oxide (ITO) substrates. We monitored the differences in the impedance recorded on the three types of electrodes: the bare electrode, the electrode coated with PLL, and the electrode seeded with HT-22 cells at DIV3 in a state of semi-confluency. All the experiments were carried out using a three-electrode set up, with Dulbecco's modified eagle medium (DMEM) complete medium serving as the electrolyte solution.

Figure 6a reports the impedance modulus plot, depicting the relationship between impedance and frequency for three different conditions: the bare P3HT substrate (shown in black), the P3HT substrate coated with PLL (represented in red) and the P3HT substrate seeded with HT-22 cells (indicated in green). Both the P3HT and PLL-coated P3HT substrates show similar trends, characterized by a slightly increase in impedance, which can be attributed to the formation of a resistive layer. In contrast, it is notable that for seeded cells on a substrate, an impedance plateau forms at lower frequency values, over the range 0 Hz <Log f < 2 Hz indicative of the formation of cell-cell tight-interactions. On the other hand, at medium to high frequencies, the impedance of the cell layer increases in comparison to the other substrates. This suggests that resistive components become more dominant probably due to the strong interaction between the cells and the substrate.

Figure 6b presents the EIS plots for P3HT-MWCNT substrates, revealing that the frequency spectra for both P3HT-MWCNT and PLL deposited on P3HT-MWCNT exhibit a remarkably similar trend. Notably, HT-22 cell impedance on the substrate displays a counterintuitive behavior; it remains consistently lower across the entire frequency range, with a significant reduction observed at higher frequency when compared to the bare substrate. Electrochemical measurements demonstrate that the presence of MWCNTs enhances electron transport and boosts charge carrier mobility. Furthermore, the nanoscale properties of MWCNTs promote cell attachment and spreading. The proximity of electroactive HT-22 cells to the P3HT-MWCNT conductive layer facilitates more efficient charge transfer and metabolic activity of the adherent cells. This efficiency, evident an intermediate to high frequency, may contribute to the observed reduction in impedance by altering the local microenvironment and promoting the formation of conductive pathways within the substrate. Supporting this, SEM-FIB images show membrane invaginations caused by the presence of MWCNT at the interface. To confirm this interpretation, optical microscopy analysis (Figure S5c,d, Supporting Information) indicate that cell

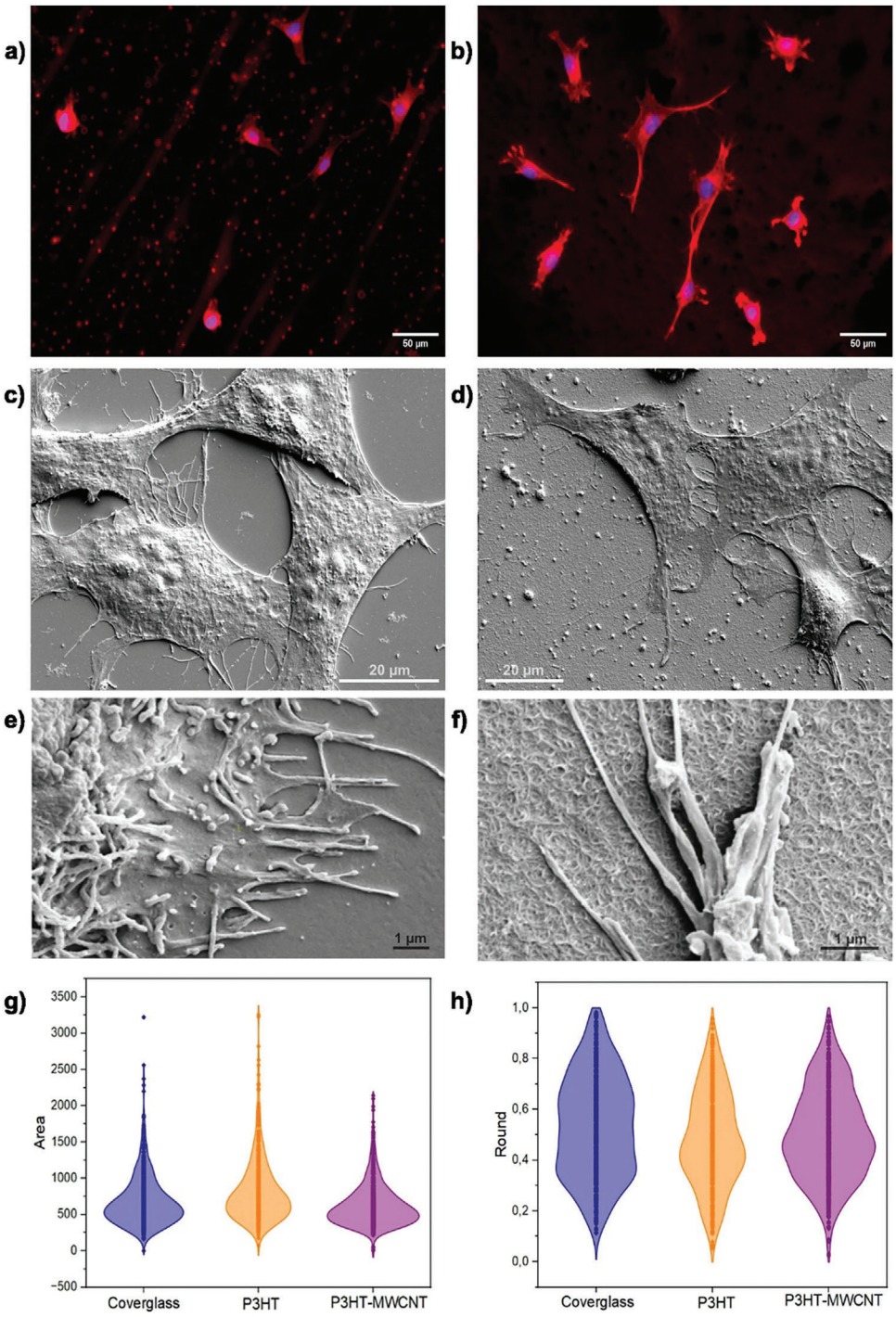

Figure 4. Morphological characterization of HT-22 cells cultured on polymers films. a) Fluorescence images of HT-22 cells on P3HT and b) on P3HT-MWCNT, acquired by fluorescence microscopy at 20x magnifications. In blue nuclei staining, in red actin staining. Scale bar, 50 µm. c) Top view scanning electron microscopy (SEM) micrographs showing HT-22cells at DIV1 on P3HT and d) P3HT-MWCNT, respectively at 5x and 4x magnifications. Scale bar, 20µm. e) Scanning electron micrographs of critically point dried (CPD) HT-22 cells on P3HT and f) on P3HT-MWCNT, respectively at 50x and 70x magnifications. Scale bar, 1µm. g) Data of area of the cells and h) roundness of the cells, obtained from ImageJ analysis of fluorescence images.

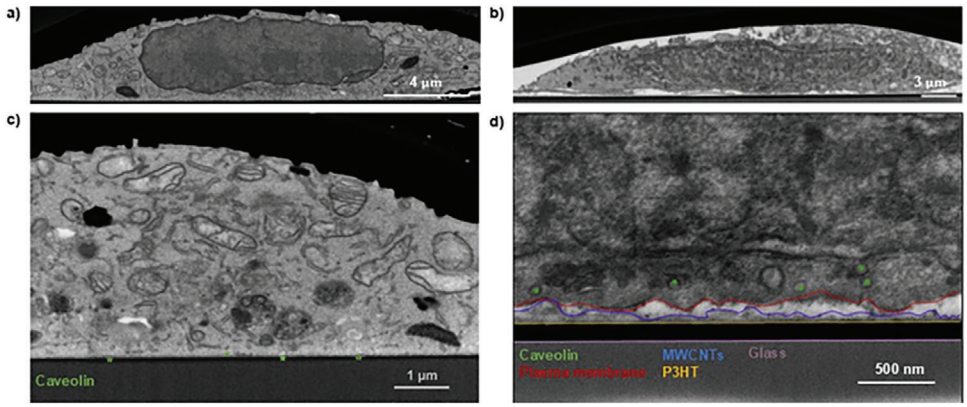

Figure 5. Interactions between HT-22 cells and polymers films substrates. Scanning electron microscopy (SEM) micrographs cross section showing the interface between HT-22 cells fixed at DIV1 and P3HT film a), c) and P3HT-MWCNT film b), d) Images to point out the adhesion point of the membrane with the MWCNT network at the interface.

detachment can be ruled out, allowing us to conclude that the observed impedance response is linked to a decrease in transcellular resistance and an improvement in communication between the cells and the electrode.

For all investigated systems the Randles circuit illustrated in Figure 6c was used for modelling. The fitted data are reported in Figure S4a–f (Supporting Information).[58]

A similar analysis was performed on bare ITO substrates, revealing a remarkable overlap of the impedance modulus curves for ITO, PLL deposited on ITO, and HT-22 cells seeded on the substrate (see Figures S6a and S7a,b, Supporting Information). These results suggest that the electrical properties of the substrate play a crucial role in the impedance measurements, suggesting that surface coverage may not dramatically affect the overall impedance. To simplify the modelling, an RC circuit was employed (Figure S6b, Supporting Information) with the fitted data reported in Figure S6c–e (Supporting Information).

In summary, the experimental evidence reported indicates that P3HT and, even more so the P3HT-MWCNT polymer blend, satisfy the requirements for excellent electrochemical properties and biocompatibility. These materials demonstrate potential as effective platforms for cellular adhesion and proliferation, promoting the formation of a neural cell networks at their interface, thereby making them suitable for application in neural interfacing and bioelectronics. Furthermore, they possess the desired softness for facilitating cell interactions as well as semi-transparency, enabling complementary analysis and monitoring through bright field using optical microscopy.

3. Conclusion

In this paper, we present a method for obtaining a blended polymer film of P3HT-MWCNT. We have examined the morphology and physico-chemical properties of the polymer films, highlighting their tunable nanostructured surface and their inherently softer qualities. The electrochemical characterization of the systems shows that incorporating MWCNT as fillers significantly enhances the conductivity and capacitance of the polymer films. Since that the stiffness of the substrate play a key role in mechanosensing of cells, the response of HT-22 cells on both P3HT and P3HT-MWCNT has been carefully investigated. To improve the cell-substrate interactions, we investigated the adsorption of Poly-L-lysine, a commonly used protein coating in cell culture, on the two substrates. Notably, we observed a significant

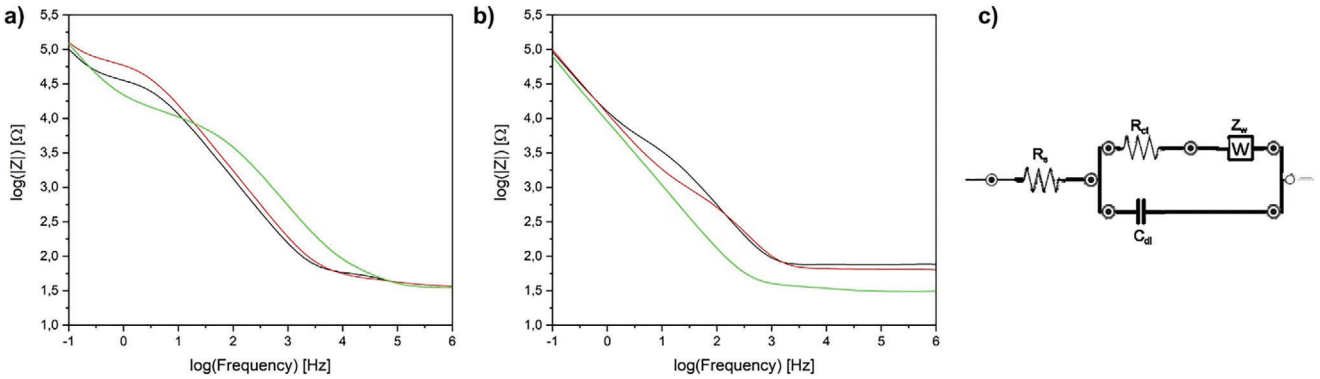

Figure 6. Cell-substrate impedance monitoring. Electrochemical impedance spectroscopy (EIS) for electrical cell-substrate impedance sensing (ECIS) of HT-22 cells at DIV3 on P3HT sample a), comparing the electrode coated with the bare polymer (in black), the protein coating of PLL (in red) and the cells layer (in green); and on P3HT-MWCNT sample b), comparing the electrode coated with the polymer blend (in black), the PLL coating (in red) and the cells layer (in green). Randles equivalent circuit c) used for the rationalization of the phenomena.

increase in mass uptake on the blend polymer film, which was associated with a more rapid adsorption kinetics. These results are particularly promising for cell culture application, as cells seeded on P3HT and P3HT-MWCNT coated with PLL exhibited an impressive, well-stretched neuronal star-like morphology in their cytoskeleton.

The study revealed a noteworthy enhancement in cell viability and proliferation over time when compared to the glass control. It highlighted the influence of the cell-material interface on the behavior of cell membrane, indicating that HT-22 cells actively respond to the surface nanostructures.

To explore the potential of P3HT-MWCNT substrate, we conducted electrochemical impedance spectroscopic measurements to evaluate its efficiency as platforms for bioelectronic applications, particularly in cell recording. Our findings suggest an intriguing approach for achieving a customizable and easily nanostructured surface of semiconductor polymers by employing MWCNT as fillers at the interface with HT-22 neuronal cells. This innovative technique holds promise for the development of electrodes for in vitro neuroelectronics applications.

4. Experimental Section

Materials and Substrates: All solvents and chemicals were of reagent quality and were used without further purifications. Regioregular poly-3-hexylthiophene (P3HT), with an average M_w 50000–100000 Da, was purchased from Sigma-Aldrich; thin multi-walled carbon nanotube (MWCNT), 95+%C purity, was purchased from Nanocyl, chloroform ($CHCl_3$) was obtained from Merck. Silicon (100) wafers from Siegert and glass substrates coated with a 100 nm layer of Indium Tin Oxide (ITO) (20 × 15 mm) from Ossila, were used as solid substrates to deposit thin polymer films.

Poly-L-lysine (PLL) solution 0.01% sterile filtered, average M_w 70000–150000 Da, Poly-L-lysine (PLL) 0.1% (w/v) in H_2O, average M_w 150000–300000 Da, and PBS (properly diluted) were purchased from Sigma-Aldrich.

Polymer Blend Preparation and Film Deposition: P3HT was dissolved in $CHCl_3$ at concentration 2.5 mg ml^{-1} and then the solution was homogenized by ultrasonic tip (Hielscher UP100H) with amplitude 50% and cycle 0.5, for 30 min in ice bath. For the preparation of the blend, P3HT and MWCNTs were weighed in a 1:1 ratio and dissolved in $CHCl_3$ at concentration of 2.5 mg ml^{-1}, sonicating the dispersion by ultrasonic tip (amplitude 50% and cycle 0.5, for 30 min in ice bath). Before film deposition, silicon wafers and ITO glasses were treated for 15 min in a UV/O_3 chamber (UV/Ozone ProCleaner, BioForce Nanosciences), rinsed with MilliQ water and dried with nitrogen, then P3HT solution or P3HT-MWCNT dispersion were deposited onto the substrates by spin coating (3500 rpm 60 s). The P3HT-MWCNT films were annealed at 120 °C for 10 min to completely remove the solvent and increase the stability of the film in the buffer solution.

Atomic Force Microscopy (AFM) Analysis: AFM analyses were carried out on thin polymer films to investigate the mechanical properties and the topography of surfaces. The Young modulus was calculated from the collected force–distance curves measured with the NTEGRA AFM (NT-MDT, Moscow, Russia). Stiff single-crystal silicon cantilevers with a symmetric tip shape were used (model Tap300Al-G, BudgetSensors, Bulgaria: nom. Frequency 300 kHz, nom. Spring constant 40 N m^{-1}, tip radius < 10 nm). The probe was calibrated measuring the cantilever spring constant by the Sader method.[59] The Young modulus was obtained by fitting experimental force–distance curves in the elastic region with Derjaguin–Müller–Toporov (DMT)[60] model using the following Equation (3):

$$F + F_{ad} = \frac{4E_s}{3\left(1-\nu_s^2\right)} R^{\frac{1}{2}} \delta^{\frac{3}{2}} \tag{3}$$

where F is the applied force; F_{ad} is the adhesion force; E_s is Young's modulus; ν_s is the Poisson's ratio for the sample; R is the radius of the spherical indenter; and δ is the elastic indentation depth. The measurements were made in triplicate, and each surface was indented in different areas, acquiring about three hundred curves for sample. From the data collected, the elastic modulus distribution was assessed with Origin 2018 software.

For morphological analysis at the nanometer scale Atomic Force Microscopy (AFM) (Multimode Nanoscope IIIA, Digital Instruments, Santa Barbara, CA) was used. Images were acquired in tapping mode using Silicon standard tapping mode AFM probes (model Tap300-G, BudgetSensors, Bulgaria: Resonant Frequency 300 kHz, Force constant 40 N m^{-1}, tip radius < 10 nm). For each sample 5, 2, 1 µm and 500 nm scan areas were acquired over different zones of the substrates surface. Images were recorded using height and phase-shift with 512 × 512 measurement points (pixels). Image processing and surface roughness analysis were performed by using Nanoscope RIII software.

The IV curves were obtained by conductive atomic force microscopy (c-AFM) and acquired with the NTEGRA AFM (NT-MDT, Moscow, Russia). Conductive tips were used (model FMG01/Pt, NT-MDT, Russia: nom. Frequency 70 kHz, nom. Force constant 3 N m^{-1}, tip radius 35 nm), and the measurements were carried out in air. More than 100 curves have been acquired analysing different zones of the samples, and from the average of the collected curves, the data were obtained and calculated with Origin 2018 software.

Quartz Crystal Microbalance with Dissipation Monitoring (QCM-D) Measurements: Measurements of adsorption kinetics were performed by using a quartz crystal microbalance with dissipation monitoring (QCM-D, Q-Sense Explorer, controlled by Q-Soft integrated software from Biolin Scientific, Gothenburg, Sweden). The measurement chamber was operating in phosphate buffer saline (PBS, 0.01 M, 0.137 M NaCl, pH 7.4) at 25 ± 0.1 °C and the flow rate was 100 µL min^{-1}. The simultaneous measurements of frequency, f, and energy dissipation, D, with time were performed in the fundamental resonance frequency ($n = 1$, f = 5 MHz) and the overtones ($n = 3, 5, 7, 9, 11$ and 13 corresponding to f = 15, 25, 35, 45, 55 and 65 MHz, respectively). The resolution in f and D was ± 0.1 Hz and 1×10^{-7},[61] respectively. Every experiment was replicated three times. In case of formation of a rigid, evenly distributed and sufficiently thin adsorbed layer, the frequency to mass conversion can be obtained by applying the Sauerbrey Equation (4):[62]

$$M = -\left(\frac{C}{n}\right) f \tag{4}$$

where f is the variation of the resonant frequency, M is the mass uptake at the sensor surface, C is a constant depending on the intrinsic properties of quartz plate (C = 17.7 ng cm^{-2} Hz^{-1} at F = 5 MHz) and n is the overtone number ($n = 1,3,5 \ldots$).

Each QCM-D experiment started with the sensor running stable in PBS for 10 min, then the addition of 300 µL PLL solution and, after 60 min, the exchange of the solution being measured with PBS at 70 and 85 min, to rinse the surface and to check both the desorption and the stability of the adsorbed layer and to remove any loosely bound residues. Phosphate-buffered saline (PBS) tablet (Sigma Aldrich) dissolved in MilliQ water was used as baseline. Poly-L-lysine (PLL) was used as purchased without any further purification.

In Vitro Studies: In vitro studies were performed by seeding cells culture on the deposited thin films of P3HT, P3HT-MWCNT, and on coverglasses as control. The coverglasses were cleaned by washing, three times, with MilliQ water for 10 min, then with acetone for 10 min and after with 2-Propanol for 10 min in ultrasound bath. Finally, they were dried with nitrogen. All the samples were sterilized for 1 h under UV, then the coating step was performed before seeding cells using Poly-L-lysine (Mw 70000–150000 Da) at a concentration of 0.01% w/v (Sigma- Aldrich) and leaving on the samples for 1 h, the excess was removed by washing it with sterilized MilliQ water.

Cell Cultures: Mouse Hippocampal Neuronal Cell Line (HT-22) were obtained from Merck Millipore (Milan, Italy). HT-22 were cultured in Dulbecco's Modified Eagle's Medium High glucose (Sigma Life Science S.r.l.,

Darmstadt, Germany), supplemented with 1% v/v L-glutamine (ThermoFisher, Waltham, MA, USA), 10% v/v Fetal Bovine Serum (FBS) (ThermoFisher, Waltham, MA, USA) and 1% v/v penicillin/streptomycin (ThermoFisher, Waltham, MA, USA) and incubated in a humidified atmosphere containing 5% CO_2 at 37 °C. The medium was replaced twice a week, and cells were split at ≈ 80% of confluence.

Cells Viability Assay: Cell viability assay was performed by MTT assay (Abcam, Cambridge, UK). 5×10^3 cells per well were cultured on the different samples and incubated in humidified atmosphere containing 5% CO_2 at 37 °C for 1,2,5 and 7 days (DIV1, DIV2, DIV5, DIV7). After this incubation time, the medium from each well was removed and replaced with 50 µl of serum-free media and 50 µl of MTT reagent and the 96-well plate incubated at 37 °C for 3 h.

After that, 150 µl of MTT solvent were added into each well and incubated 15 min. Finally, the absorbance of the solution after the interaction with the cells has been quantified by measuring it at 590 nm using a microplate reader (SpectraMax iD5 Multi-Mode, Molecular Devices). Each biological tests were performed in triplicate and for each test the samples were analysed in triplicate. The average absorbance of control at each time point was considered as 100% of cell viability, while the other samples were calculated according to the following Equation (5):

$$cell\ viability\ (\%) = \frac{Abs\_Sample}{Abs\_Control}\ x\ 100 \tag{5}$$

The MTT values were presented as average % values ± SD%.

Live-Dead and Immunofluorescence Analyses: For live/dead assay and Immunostaining 36×10^3 cells cm^{-2} were cultured on the different samples and incubated in humidified atmosphere containing 5% CO_2 at 37 °C for 1 day (DIV1).

Live/Dead assay was performed using the assay kit (Thermo Fisher, Waltham, MA, USA) with highly sensitive dyes for live cells (calcein-AM) and for dead cells (ethidium homodimer-1). Live/Dead solution was prepared adding green-fluorescent calcein-AM (5 µl) and red-fluorescent ethidium homodimer-1 (20 µl) in PBS (10 ml). Then Live/Dead solution was added to the cells seeded on the samples and incubated for 30 min at room temperature. The images were acquired using the EVOS M5000 Imaging System (Thermo Fisher Scientific, Waltham, Massachusetts, USA). ImageJ software was utilized for quantifying the number of live and dead cells, and the percentages were calculated employing the following Equations (6) and (7):

$$Number\ of\ live\ cells\ (\%) = \frac{(Live\ cells)}{(Live\ cells + Dead\ cells)}\ x\ 100 \tag{6}$$

$$Number\ of\ dead\ cells\ (\%) = \frac{(Dead\ cells)}{(Live\ cells + Dead\ cells)}\ x\ 100 \tag{7}$$

Immunofluorescence analysis was performed as follow. After fixation with 4% Paraformaldehyde (PFA) for 20 min at room temperature (Società Italiana Chimici, Rome, Italy), cell membranes were permeabilized to allow the access at the antibodies to the targets in 0.1% Triton-X 100 for 15 min at room temperature. To prevent any non-specific binding of the antibody, specimens were incubated in 2% bovine serum albumin (BSA) in PBS for 45 min at room temperature and then incubated with conjugated antibody Phalloidin-647 diluted (1:1000) (Abcam, Cambridge, UK) in 2% BSA in PBS for 40 min for actin filaments staining. After washing the samples with PBS, nuclei were counterstained with Hoechst solution (1:2000) (ThermoFisher, Waltham, MA, USA) in PBS for 10 min and finally the samples were mounted with glycerol 50% in H_2O and sealed on the glass slide with biocompatible biphasic glue. Samples were shielded from light until imaging, and kept at 4 °C. The images were acquired using fluorescence microscope (ApoTome Fluorescen Microscope Axio Imager Z1, ZEISS). Measurements involving cell area, minor and major axis length were conducted using ImageJ, the cell morphological features were presented as average area covered by cells and roundness, determined by the ratio of major axis to minor axis.

Focused Ion Beam Scanning Electron Microscopes (FIB-SEM) Analysis: For FIB/SEM analysis 36×10^3 cells cm^{-2} were cultured on the different samples and incubated in humidified atmosphere containing 5% CO_2 at 37 °C for 1 day (DIV1). The cells were analyzed at DIV1 after fixation.

Ultra-Thin Plasticization Procedure (UTP): Specimens were chemically fixed in 4% v/v paraformaldehyde (Società Italiana Chimici, Rome, Italy) dissolved in water milli-Q, then in 2.5% v/v glutaraldehyde (Electron Microscopy Science, Hatfield, PA) diluted in 0.1 M cacodylate buffer (Electron Microscopy Science, Hatfield, PA) overnight at 4 °C. Subsequently, samples were washed with a 0.1 M cacodylate solution.[63,64] During these steps, the samples were kept on ice. The buffer solution was then replaced with 20 mM Glycine (prepared in sodium cacodylate 0.1 M) and kept for 20 min. Afterward, the samples were incubated in a solution with 4% v/v aqueous osmium tetroxide (Electron Microscopy Science, Hatfield, PA) and 2% potassium ferrocyanide (Electron Microscopy Science, Hatfield, PA) for 1 h at 4 °C, away from direct light. Samples were then washed three times with 0.1 M cacodylate buffer solution. A final incubation with 2% v/v osmium tetroxide (Electron Microscopy Science, Hatfield, PA) aqueous solution was performed at room temperature for 30 min. Specimens were rinsed with DI water at room temperature and then immersed in 1% w/v filtered thiocarbohydrazide (TCH) (Electron Microscopy Science, Hatfield, PA) in DI water for 20 min at room temperature. Subsequently, the samples were washed three times in DI water, and then they were incubated overnight at 4 °C *en bloc* staining solution in 4% v/v uranyl acetate. Afterward, they were rinsed again three times with DI water and then kept in 0.15% v/v tannic acid solution (Sigma Aldrich), for 3 min at 4 °C. The dehydration was carried out in a series of ethanol dilutions (30% v/v, 50% v/v, 75% v/v, 2×95% v/v, 100% v/v, ethanol in water) for 10 min at 4 °C. In addition, the samples were washed twice with 100% v/v ethanol. Finally, they were immersed with a resin solution within different ethanol:resin ratios (2:1, 1:1, 1:2), where the resin is composed by Nonenyl Succinic Anhydride (NSA) (25 mL), Diglycidyl Ether of Polypropylene (D.E.R. 736) (8 mL), Epoxycyclohexanemethyl 3,4-epoxycyclohexanecarboxylate (ERL 4221) (10 mL), Dimethylaminoethanol (DMAE), Electron Microscopy Science) (301 µL). At the end, the samples were embedded in absolute resin, overnight and over-day with several changes.

Therefore, the specimens were put in a vertical position for 3 h and then polymerized for 24 h at 70 °C. Samples were mounted onto aluminum stubs (diameter = 3.2 mm) using silver conductive paste (RS Pro) and sputtered with a 15 nm thick golden layer prior to imaging.

Critical Point Drying (CPD): Cells were fixed with 4% v/v paraformaldehyde (Società Italiana Chimici, Rome, Italy) followed by 2.5% v/v glutaraldehyde (Società Italiana Chimici, Rome, Italy) diluted in 0.1 M sodium cacodylate buffer solution (Società Italiana Chimici, Rome, Italy) for 1h. Then the samples were incubated keeping the temperature at 4 °C, and 20 mM glycine (Merck Life Science S.r.l., Milan, Italy) solution is added and kept for 20 min. Then, to stain the membrane, the sample were incubated at 4 °C for 1 h in a solution of 2% v/v of osmium tetroxide (Società Italiana Chimici, Rome, Italy) and 2% v/v potassium ferrocyanide (Società Italiana Chimici, Rome, Italy). The dehydration was accomplished by different incubations of ethanol for 5 min at 4 °C. The ethanol concentration was increased from 30%v/v of ethanol diluted in water, then 50% v/v, 75%v/v, 85% v/v, 95% v/v, and three times 100% v/v of ethanol. Then, the solvent is exchanged with liquid which is let evaporate by temperature increase until no liquid components are present. The sample surface is then coated with a thin layer of metal (15 nm) and then ready for the imaging.

Scanning Electron Microscopy (SEM): SEM imaging was carried out using Helios CX 5 field emission gun (FEG) SEM, the samples were images in secondary electron mode (SE mode) acceleration voltages in the range of 3 kV and current 0.17 nA and a working distance of 4mm.

Scanning Electron Microscopy – Focused Ion Beam (SEM-FIB): The specimens were loaded inside the dual-beam vacuum chamber (Thermo Fisher, Helios CX 5). The region of interest (ROI) was detected. One deposition layer was performed, by ion beam deposition (0.5 µm thickness of platinum, with current 0.43 nA and tension 30 kV). Cross sections were performed by first trenching out the material via an ion beam (cutting thickness: 4 µm; current: 0.79 nA; tension: 30 kV). The ion beam was then used to polish the interface (current: 0.23–0.43 nA; tension: 30 kV).

Scanning electron micrographs were acquired in backscattered mode with a dwell time of 10 µs, at high resolution and the electron beam to 3 kV and current 0.17 nA.

Electrochemical Characterization: The electrochemical characterization of the films was carried out using a three electrode cells configurated with Ag/AgCl as reference electrode and Pt wire as counter electrode (Redox.me, Sweden), in PBS as electrolyte solution to better mimic the physiological conditions. The analysis performed were Electrochemical Impedance spectroscopy (EIS) and Cyclic voltammetry (CV), and the instrument used was VSP-300 Potentiostat (BioLogic Science Instruments, Seyssinet-Pariset France). For EIS analysis the parameters were set with an initial potential of 0 V versus reference, the frequency range scanned was between 1 MHz and 0.1 Hz with a potential amplitude of 50 mV. The CV parameters were set with set with an initial potential of 0 V versus reference, the potential range analysed was between −1.5 and 1.5 V, with a scan rate of 100 mV s^{-1}. For every experiment the measurement was repeated for several cycles between 3 and 5, and each measurement was made in triplicate. All the electrochemical analysis were performed in a Faraday cage. The collected data were analysed using Origin 2018 software, and the EIS curves fitting was performed by means of Python-based script using Python 3.1.

Data Analysis: AFM images were flattened with the Digital Instrument software version 4.23r6 tool to remove the background slopes and using the same software the roughness analysis was carried out. The roughness averaged values were obtained considering the values obtained for a minimum of six separate zones for each sample from different regions of the substrate. The data were presented as mean ± standard deviation. The Young's modulus was calculated by fitting experimental curves with the DMT model in the elastic region, using the FCprocessor2 of the NovaPx software. Five hundred force-distance curves were acquired indenting each surface in different areas, the measurements were made in triplicate. The presented values were calculated considering the maximum value of the LogNormal distribution of the obtained values.

From the QCM-D experiments, the frequency shift and the dissipation change were obtained by the average of all the overtones recorded, considering the variation between the initial steady state and the values reached after the washing steps at the end of the monitored adsorption. By applying the Sauerbrey equation for the frequency-to-mass conversion, the adsorbed mass was obtained. For PLL adsorption the number of molecules adsorbed per cm^2 was obtained considering the average molecular weight of the protein provided by the company. The data were presented as mean ± standard deviation. All the QCM-D measurements were performed in triplicate.

The adsorption kinetic constants were obtained considering the RSA model. The apparent diffusion coefficient (S) was calculated by the slope of the diffusion-controlled step from the plot of the mass uptake calculated for the third overtone of the resonance frequency versus the square root of the adsorption time expressed in hours. The average mass transfer rate constant (kc) was calculated considering the S value obtained. The kinetic parameters were obtained by using the more sensitive frequency overtone (F3).

CV and IV curves were analyzed using Origin 2018 software, and the EIS curves fitting was performed by means of Python-based script using Python 3.1.

Statistical Biological Data Analysis: Three parallel cultures were prepared for each substrate and every experiment was repeated three times ($n = 3$). Data were analysed either as raw data or as mean ± standard deviation (SD), as appropriate. Differences between several time points of each experiment timeline were evaluated by using one/two-way ANOVA with post hoc Holm test, where appropriate. $p < 0.05$ was considered significant.

Supporting Information

Supporting Information is available from the Wiley Online Library or from the author.

Acknowledgements

F.S. and P.C. thank Velia Siciliano's lab – Istituto Italiano di Tecnologia, Italy for kindly provided HT-22 cells. P.C. and F.S. thank Dr. Claudia Lubrano, Dr. Ziyu Gao for the help provided for preliminary consideration on cell culture studies, and Dr. Ugo Bruno for the help for EIS fitting.

Open access publishing facilitated by Universita degli Studi di Catania, as part of the Wiley - CRUI-CARE agreement.

Conflict of Interest

The authors declare no conflict of interest.

Data Availability Statement

The data that support the findings of this study are available from the corresponding author upon reasonable request.

Keywords

bioelectronics, biointerfaces, carbon nanotubes, cell culture, cell-chip coupling, neuroelectronics, P3HT

Received: October 28, 2024
Revised: January 24, 2025
Published online:

[1] J. B. Kaushal, P. Raut, S. Kumar, *Biosensors* **2023**, *13*, 976.
[2] D. T. Simon, E. O. Gabrielsson, K. Tybrandt, M. Berggren, *Chem. Rev.* **2016**, *116*, 13009.
[3] J. K. Trevathan, I. Baumgart, E. N. Nicolai, B. A. Gosink, A. J. Asp, M. L. Settell, S. R. Polaconda, K. Malerick, S. K. Brodnick, W. Zeng, B. E. Knudsen, A. L. McConico, Z. Sanger, J. H. Lee, J. M. Aho, A. J. Suminski, E. K. Ross, J. L. Lujan, D. J. Weber, J. C. Williams, M. Franke, K. A. Ludwig, A. J. Shoffstall, *bioRxiv* **2019**, *21*, 584995.
[4] J. Rivnay, R. M. Owens, G. G. Malliaras, *Chem. Mater.* **2014**, *26*, 679.
[5] M. Berggren, A. O. B Richter-Dahlfors, *Adv. Mater.* **2007**, *19*, 3201.
[6] C. Pitsalidis, A.-M. Pappa, A. J. Boys, Y. Fu, C.-M. Moysidou, D. van Niekerk, J. Saez, A. Savva, D. Iandolo, R. M. Owens, *Chem. Rev.* **2022**, *122*, 4700.
[7] G. G. Malliaras, *Biochim. Biophys. Acta BBA – Gen. Subj.* **2013**, *1830*, 4286.
[8] S. Lee, B. Ozlu, T. Eom, D. C. Martin, B. S. Shim, *Biosens. Bioelectron.* **2020**, *170*, 112620.
[9] O. Bettucci, G. M. Matrone, F. Santoro, *Adv. Mater. Technol.* **2022**, *7*, 2100293.
[10] S. O. Alaswad, A. S. Mahmoud, P. Arunachalam, *Polymers* **2022**, *14*, 4924.
[11] J. Kappen, M. Skorupa, K. Krukiewicz, *Biosensors* **2022**, *13*, 31.
[12] S. Fabiano, L. Flagg, T. C. H. Castillo, S. Inal, L. G. Kaake, L. V. Kayser, S. T. Keene, S. Ludwigs, C. Muller, B. M. Savoie, B. Lüssem, J. L. Lutkenhaus, M. Matta, D. Meli, S. N. Patel, B. D. Paulsen, J. Rivnay, J. Surgailis, *J. Mater. Chem. C* **2023**, *11*, 14527.
[13] S. G. Higgins, A. Lo Fiego, I. Patrick, A. Creamer, M. M. Stevens, *Adv. Mater. Technol.* **2020**, *5*, 2000384.
[14] D. O. Adewole, M. D. Serruya, J. A. Wolf, D. K. Cullen, *Front. Neurosci.* **2019**, *13*, 269.
[15] G.-T. Go, Y. Lee, D.-G. Seo, T.-W. Lee, *Adv. Mater.* **2022**, *34*, 2201864.
[16] P. Jastrzebska-Perfect, S. Chowdhury, G. D. Spyropoulos, Z. Zhao, C. Cea, J. N. Gelinas, D. T. N Khodagholy, *Adv. Funct. Mater.* **2020**, *30*, 1909165.

[17] S. T. Keene, C. Lubrano, S. Kazemzadeh, A. Melianas, Y. Tuchman, G. Polino, P. Scognamiglio, L. Cinà, A. Salleo, Y. van de Burgt, F. A. B Santoro, *Nat. Mater.* **2020**, *19*, 969.
[18] H. Yi, R. Patel, K. D. Patel, L.-S. Bouchard, A. Jha, A. W. Perriman, M. Patel, *J. Mater. Chem. B* **2023**, *11*, 11006.
[19] F. Zha, W. Chen, L. Hao, C. Wu, M. Lu, L. Zhang, D. Yu, *Soft Matter* **2020**, *16*, 6591.
[20] S. Bellani, D. Fazzi, P. Bruno, E. Giussani, E. V. Canesi, G. Lanzani, M. R. Antognazza, *J. Phys. Chem. C* **2014**, *118*, 6291.
[21] E. Mosconi, P. Salvatori, M. I. Saba, A. Mattoni, S. Bellani, F. Bruni, B. Santiago Gonzalez, M. R. Antognazza, S. Brovelli, G. Lanzani, H. Li, J. L. Brédas, F. De Angelis, *ACS Energy Lett.* **2016**, *1*, 454.
[22] A. Mariano, C. Lubrano, U. Bruno, C. Ausilio, N. B. Dinger, F. Santoro, *Chem. Rev.* **2022**, *122*, 4552.
[23] A. de la Zerda, M. J. Kratochvil, N. A. Suhar, S. C. Heilshorn, *APL Bioeng.* **2018**, *2*, 021501.
[24] S. Song, D. Amores, C. Chen, K. McConnell, B. Oh, A. Poon, P. M. George, *Sci. Rep.* **2019**, *9*, 19565.
[25] J. C. Fontoura, C. Viezzer, F. G. dos Santos, R. A. Ligabue, R. Weinlich, R. D. Puga, D. Antonow, P. Severino, C. Bonorino, *Mater. Sci. Eng. C* **2020**, *107*, 110264.
[26] A. Mariano, C. L. Bovio, V. Criscuolo, F. Santoro, *Nanotechnology* **2022**, *33*, 492501.
[27] F. A. Pennacchio, L. D. Garma, L. Matino, F. Santoro, *J. Mater. Chem. B* **2018**, *6*, 7096.
[28] D. Baruffaldi, G. Palmara, C. Pirri, F. Frascella, *ACS Appl. Bio Mater.* **2021**, *4*, 2233.
[29] A. Hai, D. Kamber, G. Malkinson, H. Erez, N. Mazurski, J. Shappir, M. E. Spira, *J. Neural Eng.* **2009**, *6*, 066009.
[30] H. Teixeira, C. Dias, P. Aguiar, J. Ventura, *Adv. Mater. Technol.* **2021**, *6*, 2000770.
[31] M. E. Spira, N. Shmoel, S.-H. M. Huang, H. Erez, *Front. Neurosci.* **2018**, *12*, 00212.
[32] F. Milos, A. Belu, D. Mayer, V. Maybeck, A. Offenhäusser, *Adv. Biol.* **2021**, *5*, 2000248.
[33] G. M. L. Messina, C. Satriano, G. Marletta, *Chem. Commun.* **2008**, *40*, 5031.
[34] A. Karakeçili, G. M. L. Messina, M. Ç. Yurtsever, M. Gümüşderelioğlu, G. Marletta, *Colloids Surf. B Biointerfaces* **2014**, *123*, 39.
[35] J. Liu, L. Li, W. Z. Suo, *Life Sci.* **2009**, *84*, 267.
[36] G. Scarpa, A.-L. Idzko, S. Götz, S. Thalhammer, *Macromol. Biosci.* **2010**, *10*, 378.
[37] E. M. Elsehly, E. M. M. Ibrahim, M. A. El-Hadek, A. El-Khouly, V. Khovaylo, Z. M. Elqahtani, N. G. Chechenin, A. M. Adam, *Phys. E Low-Dimens. Syst. Nanostructures* **2023**, *146*, 115566.
[38] C. F. Guimarães, L. Gasperini, A. P. Marques, R. L. Reis, *Nat. Rev. Mater.* **2020**, *5*, 351.
[39] Y. Liu, A. F. McGuire, H.-Y. Lou, T. L. Li, J. B.-H. Tok, B. Cui, Z. Bao, *Proc. Natl. Acad. Sci. USA* **2018**, *115*, 11718.
[40] U. A. Aregueta-Robles, A. J. Woolley, L. A. Poole-Warren, N. H. Lovell, R. A. Green, *Front. Neuroeng.* **2014**, *7*, 15.
[41] A. Carnicer-Lombarte, D. G. Barone, I. B. Dimov, R. S. Hamilton, M. Prater, X. Zhao, A. L. Rutz, G. G. Malliaras, S. P. Lacour, C. E. Bryant, J. W. Fawcett, K. Franze, *bioRxiv* **2022**, *28*, 829648.
[42] P. Acevedo-Peña, A. Baray-Calderón, H. Hu, I. González, V. M. Ugalde-Saldivar, *J. Solid State Electrochem.* **2017**, *21*, 2407.
[43] R. Gonçalves, E. Pereira, L. Marchesi, *Int. J. Electrochem. Sci.* **2017**, *12*, 1983.
[44] B. Endrődi, G. F. Samu, M. A. Azam, C. Janáky, C. Visy, *J. Solid State Electrochem.* **2016**, *20*, 3179.
[45] H. Cui, X. Xie, S. Xu, L. L. H. Chan, Y. Hu, *Biomed. Eng. Online* **2019**, *18*, 86.
[46] J. E. B. Randles, *Discuss. Faraday Soc.* **1947**, *1*, 11.
[47] A. T. Almeida, M. C. Salvadori, D. F. S. Petri, *Langmuir* **2002**, *18*, 6914.
[48] K. Kubiak, Z. Adamczyk, M. Oćwieja, *Langmuir* **2015**, *31*, 2988.
[49] T. Mosmann, *J. Immunol. Methods* **1983**, *65*, 55.
[50] C. J. An, Y. C. Lee, Y. H. Kang, S. Y. Cho, *Carbon* **2017**, *124*, 662.
[51] P. Rathore, C. M. S. Negi, A. Yadav, A. S. Verma, S. K. Gupta, *Optik* **2018**, *160*, 131.
[52] I. Giaever, C. R. Keese, *Nature* **1993**, *366*, 591.
[53] Y. Xu, X. Xie, Y. Duan, L. Wang, Z. Cheng, J. Cheng, *Biosens. Bioelectron.* **2016**, *77*, 824.
[54] A. Elghajiji, X. Wang, S. D. Weston, G. Zeck, B. Hengerer, D. Tosh, P. R. F. Rocha, *Adv. Biol.* **2021**, *5*, 2100330.
[55] E. Primiceri, M. S. Chiriacò, R. E. Ionescu, E. D'Amone, R. Cingolani, R. Rinaldi, G. Maruccio, *Microelectron. Eng.* **2009**, *86*, 1477.
[56] K. Krukiewicz, *Electrochem. Commun.* **2020**, *116*, 106742.
[57] A. Niaraki, M. C. McNamara, R. Montazami, N. N. Hashemi, *ACS Appl. Bio Mater.* **2022**, *5*, 113.
[58] C. Hu, G. Wei, F. Zhu, A. Wu, L. Luo, S. Shen, J. Zhang, *ACS Appl. Bio Mater.* **2022**, *5*, 3038.
[59] J. E. Sader, J. W. M. Chon, P. Mulvaney, *Rev. Sci. Instrum.* **1999**, *70*, 3967.
[60] B. V. Derjaguin, V. M. Muller, Y. P. Toporov, *J. Colloid Interface Sci.* **1975**, *53*, 314.
[61] M. Rodahl, F. Höök, B. Kasemo, *Anal. Chem.* **1996**, *68*, 2219.
[62] G. Sauerbrey, *Z. Für Phys.* **1959**, *155*, 206.
[63] F. Santoro, W. Zhao, L.-M. Joubert, L. Duan, J. Schnitker, Y. van de Burgt, H.-Y. Lou, B. Liu, A. Salleo, L. Cui, Y. Cui, B. Cui, *ACS Nano* **2017**, *11*, 8320.
[64] C. L. Bovio, V. Mollo, A. Mariano, F. Santoro, *Neuronal Morphogenesis: Methods and Protocols*, (Eds: K. Toyooka), Springer, New York **2024**, pp. 11–20.